

Perceptual Assessment and Optimization of High Dynamic Range Image Rendering

Peibei Cao,
City University of Hong Kong
peibeicao2-c@my.cityu.edu.hk

Rafał K. Mantiuk
University of Cambridge
rkm38@cam.ac.uk

Kede Ma
City University of Hong Kong
kede.ma@cityu.edu.hk

Abstract

High dynamic range (HDR) imaging has gained increasing popularity for its ability to faithfully reproduce the luminance levels in natural scenes. Accordingly, HDR image quality assessment (IQA) is crucial but has been superficially treated. The majority of existing IQA models are developed for and calibrated against low dynamic range (LDR) images, which have been shown to be poorly correlated with human perception of HDR image quality. In this work, we propose a family of HDR IQA models by transferring the recent advances in LDR IQA. The key step in our approach is to specify a simple inverse display model that decomposes an HDR image to a set of LDR images with different exposures, which will be assessed by existing LDR quality models. The local quality scores of each exposure are then aggregated with the help of a simple well-exposedness measure into a global quality score for each exposure, which will be further weighted across exposures to obtain the overall quality score. When assessing LDR images, the proposed HDR quality models reduce gracefully to the original LDR ones with the same performance. Experiments on four human-rated HDR image datasets demonstrate that our HDR quality models are consistently better than existing IQA methods, including the HDR-VDP family. Moreover, we demonstrate their strengths in perceptual optimization of HDR novel view synthesis.

1. Introduction

High dynamic range (HDR) images aim to faithfully reproduce the large luminance variations of natural scenes that low dynamic range (LDR) images are not capable of [20]. In the past few years, plenty of HDR imaging and display devices have been developed and commercialized in response to the ever-growing need for HDR images in various fields, including photography, gaming, film, and virtual reality industries. This makes HDR image quality assessment (IQA) a practically demanding technique to monitor,

ensure, and optimize the perceptual quality of HDR images during imaging, compression, communication, and rendering.

Currently, HDR IQA models are largely lacking, which stems probably from the biased view that most LDR IQA models, such as the peak signal-to-noise ratio (PSNR) and the structural similarity (SSIM) index [64], are directly applicable to HDR images. It is only until recently that researchers realized their poor account for human perception of HDR image quality [14, 18]. Mantiuk *et al.* [33] made one of the first attempts by extending the classic visual difference predictor (VDP) [12] to HDR-VDP, which was later improved from various psychophysical and physiological perspectives [34, 36, 46]. Although the HDR-VDP family captures many aspects of the early visual system, they contain complex and non-differentiable modules, which may hinder their wide applications, especially in perceptual optimization scenarios as loss functions.

Other efforts have been put into transforming linear luminances into a perceptually more uniform space to improve the applicability of LDR quality models to HDR images. Representative transformations include the logarithmic function [65], the perceptually uniform (PU) encoding curve [1] and its improved version, PU21 encoding [30], and the perceptual quantizer [42]. One subtlety here is that most LDR IQA models are designed to accept as input display-encoded digital pixel values (e.g. in sRGB space) without converting them into luminance values using a display model (see Fig. 1). As a consequence, a direct application of these LDR quality models to process luminance values after perceptually uniform transformations are bound to be suboptimal.

Inspired by the seminal work of Munkberg *et al.* [43], we propose a family of full-reference HDR IQA models, which leverage the recent advances in LDR IQA and unify perceptual quality assessment of HDR and LDR images. At the core of our approach is the specification of a simple inverse display model [31], which decomposes and maps an HDR image in (uncalibrated) luminance values to an LDR image stack of different exposures in digital pixel val-

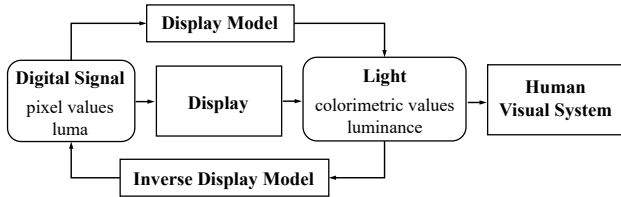


Figure 1. Forward display model simulates the process of converting digital pixel values into physical light in luminances on a display. An inverse display model provides the inverse mapping.

ues. By doing so, we are able to focus on different portions of luminance ranges for reliable LDR quality assessment. The local quality scores of each exposure are aggregated into a global quality score using a simple well-exposedness measure. The global quality scores can be further weighted across exposures to emphasize particular luminance ranges. When assessing LDR images, a corresponding display model is assumed to compensate the mapping by the inverse display model so that the capabilities of base LDR IQA models are inherited. Experiments on four human-rated HDR image datasets verify the superiority of the proposed IQA models in evaluating HDR image quality, compared to existing methods, including the HDR-VDP family.

Moreover, we demonstrate the use of the proposed HDR IQA models as the perceptual optimization objectives in HDR novel view synthesis. We simplify the method in [21], and train a multi-layer perceptron (MLP) to recover the HDR neural radiance field (NeRF). We intentionally pursue possibly simple computational structures to use the proposed HDR quality models as perceptual loss functions. Extensive comparisons on a variety of HDR scenes show that the optimized methods generally exhibit better reconstruction and synthesis performance than existing algorithms. More importantly, we observe significant visual quality improvement for over-exposed regions, which is supported by subjective user studies and objective quality estimates.

In summary, our contributions include:

- a family of HDR quality models that unify HDR and LDR IQA with demonstrated advantages in terms of correlation with human data on four databases and optimization of an HDR image rendering task;
- a simple and effective HDR novel view synthesis method, that outperforms its state-of-the-art counterpart by a clear margin.

2. Related Work

In this section, we review two bodies of studies that are related to ours, HDR IQA and HDR novel view synthesis.

2.1. HDR Quality Models

2.1.1 Model-based Methods

Model-based methods rely on computational models that mimic the physiological responses of neurons in the human visual system, especially the primary visual cortex. HDR-VDP [33] is an excellent example by extending the classic VDP [12] to take into account the aspects of non-linear photoreceptor response to light, contrast sensitivity, and local adaptation. Like VDP, HDR-VDP focuses on predicting visible difference maps without supplying a single-valued quality prediction. HDR-VDP-2 [34] improves upon HDR-VDP with a revised model of an early visual system. The metric was trained on two LDR datasets (*i.e.*, LIVE [56] and TID2008 [50]) to provide a single scalar as the prediction of the overall image quality. Quality predictions were further improved in HDR-VDP-2.2 [46], which was retrained on two additional HDR datasets: Narwaria2013 [44] and Narwaria2014 [45]. HDR-VDP-3 [36] was developed by simulating the effect of aging on the visual system [32], modeling the effect of adaptation to local luminance [62], and recalibrating the metric on the largest HDR image quality dataset - UPIQ [38]. Other representative model-based methods include HDR video quality measure (HDR-VQM) [47] and normalized Laplacian pyramid distance (NLPD) [24]. Like the HDR-VDP family, HDR-VQM follows an error visibility approach by incorporating the PU encoding as the front processing. NLPD was originally developed to compare two images of different dynamic ranges (*e.g.*, evaluating an LDR image using its corresponding HDR image as reference) by introducing divisive normalization as a form of local gain control [7].

2.1.2 Encoding-based Methods

Encoding-based methods transform linear luminances into a perceptually more uniform space to improve the applicability of LDR quality models for assessing HDR images. Xu *et al.* [65] operated on the log scale with the assumption that the luminance response curve is approximately logarithmic. Later, the PU encoding [1] was derived from the contrast sensitivity function (CSF) in [12], which was optimized to approximate gamma-encoding within the range from 0.1 to 80 cd/m^2 . Similarly, the perceptual quantizer in [42] was based on the Barten's CSF [4], and was standardized in the ITU-R Recommendation BT.2100 as the electro-optical transfer function for HDR content. As an improvement of the PU encoding [1], PU21 encoding [30] relied on a new CSF [35], predicting contrast thresholds at luminance levels between 0.0002 and 10,000 cd/m^2 . Nevertheless, the PU encoding was typically designed for the luminance channel while disregarding color information.

Our family of HDR quality models fall naturally in

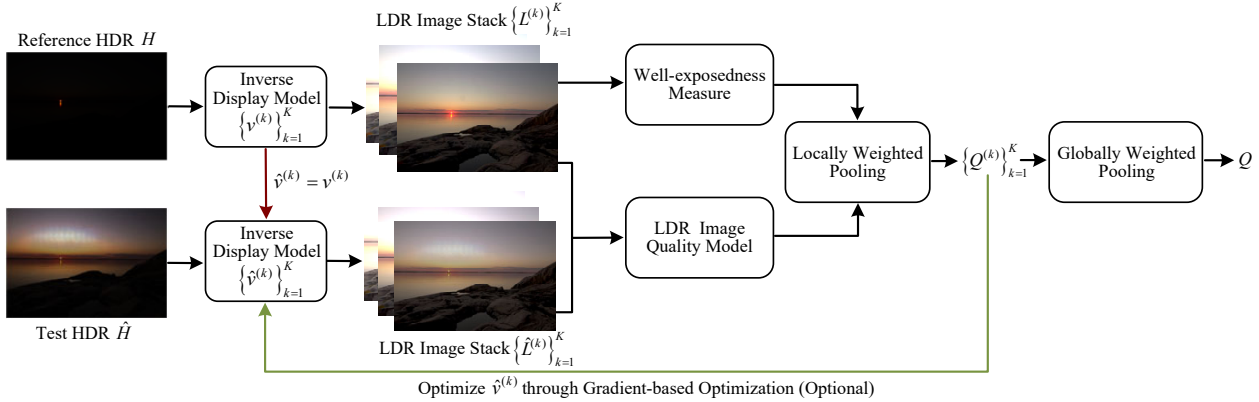


Figure 2. System diagram of the proposed family of HDR IQA models. The default red arrow can be replaced by the optional green arrow, whose goal is to compensate the possible luminance shift between the reference and test HDR images, similar as the global luminance correction in [14, 18]. Source image by courtesy of Param Hanji [18].

the category of the encoding-based methods. Inspired by Munkberg *et al.* [43], we “encode” an HDR image to a multi-exposure LDR image stack for quality assessment, without the need of HDR image data for re-calibration. Moreover, our models provide the option to account for the possible luminance shift between the two HDR images [14, 18], which are perceptually acceptable but may significantly bias computational prediction. Meanwhile, local and global weightings are considered to exclude invalid local regions and to highlight specific dynamic regions of interest, respectively, during quality assessment.

2.2. Novel View Synthesis

Novel view synthesis is a typical application of image-based rendering that involves generating images from novel viewpoints given a set of input views [57]. The view synthesis can be performed directly in the pixel domain when the input images are densely sampled [17, 25]. It is more common and economic to capture inputs from a wider range of sparse locations, which will be processed through a “proxy” geometry using either a heuristic [6] or learned blending function [19, 53, 54].

In the past few years, DNNs have become popular in the field of novel view synthesis, which can be roughly categorized into three types based on scene representations. In the first type, DNNs are combined with voxel grid representations [10, 28, 59] to reduce discretization (*i.e.* grid-like) artifacts. The second type involves training a CNN to generate multi-plane images and rendering novel views through alpha-compositing [11, 16, 39, 70]. The third type is NeRF, which represents a scene with a neural radiance field [2, 5, 9, 26, 29, 37, 40, 66]. Mildenhall *et al.* [40] demonstrated that neural implicit representations give higher-quality view synthesis results than traditional explicit representations, like point clouds, vox-

els, and octrees. Later on, various aspects of NeRF have been improved, including rendering quality and capability [2, 3, 69], training and rendering efficiency, robustness to varying illumination, transient occluders [37], and deformable objects [49], generalization to novel scenes [8], compositionality [48], and editability [27].

Recently, NeRF has been extended to work with HDR image data [21, 41]. Mildenhall *et al.* [41] trained Mip-NeRF [2] using the linear noisy RAW images. Huang *et al.* [21] modeled the physical imaging process with two implicit functions: a radiance field and a tone mapper, which are jointly optimized using multiple LDR images with different exposures as input. In this paper, we simplify the method in [21] by stripping off the tone mapper, and directly optimizing the RAW radiance field for the proposed HDR quality model, leading to noticeable perceptual gains.

3. Proposed HDR Quality Models

Motivated by the lack of HDR quality models for both quality assessment and perceptual optimization, we propose to convert the problem of HDR IQA to an LDR one with the help of a simple inverse display model [31]. This leads to a family of HDR quality models that 1) transfer the recent advances in LDR IQA, 2) require no human-rated HDR image dataset for re-calibration, and 3) unify HDR and LDR IQA. Fig. 2 shows the system diagram.

3.1. Inverse Display Model

A forward display model simulates how the display transforms digital pixel values to physical units of light, while the opposite mapping from physical units to digital values, is referred to as an inverse display model, as illustrated in Fig. 1. Here, we resort to a simple inverse display model, which was originally used by Mantiuk and Heidrich [31] for

visualizing HDR images in a web browser:

$$L^{(k)} = \left(\left[\frac{H \cdot v^{(k)} - b}{1 - b} \right]^1 \right)^{\frac{1}{\gamma}}. \quad (1)$$

$v^{(k)}$, for $1 \leq k \leq K$, is the k -th exposure value, determining the position of the dynamic range window to be mapped to the available luminance range of the display. We assume a fixed display device with the minimum and maximum luminances of $I_{\min} = 1 \text{ cd/m}^2$ and $I_{\max} = 200 \text{ cd/m}^2$, respectively, which are typical specifications of consumer-grade displays of standard dynamic ranges, resulting in the window size $w = \log_2(200/1) = 7.64$ in logarithmic scale. H denotes the reference HDR image, and $L^{(k)}$ represents the k -th LDR image. b indicates the black-level factor, accounting for the limited contrast of the display due to the light leakage and the ambient light reflections from the display. $[\cdot]_0^1$ denotes the clamping function with the output range $[0, 1]$. $(\cdot)^{1/\gamma}$ represents the gamma correction. We follow the setting in [31], and set $b = 1/128$ and $\gamma = 2.2$. Eq. (1) is independently applied to the three color channels.

It is noteworthy that we intentionally do not use state-of-the-art tone mapping operators (TMOs) for the HDR-to-LDR conversion because they are essentially dynamic range compressors, which inevitably suffer from information loss and algorithm-dependent artifacts. In contrast, the adopted inverse display model incurs minimal contrast distortions by the windowing technique, where a portion of the luminance range is mapped to that of the LDR display. Moreover, it can be seen as a local dynamic range magnifier, “zooming in” a certain luminance range for more detailed comparison.

Next, we describe how to determine the positions of the sliding windows (*i.e.*, the values of $\{v^{(k)}\}$). Following [31], we uniformly select three exposures for every eight stops¹ to cover the full luminance range. Fig. 3 (a) shows the histogram of an HDR image with eight stops as an example. We divide the eight stops into three equal dynamic ranges, and set the endpoint of the k -th window to be

$$l^{(k)} = l_0 + \frac{8}{3}k, \quad (2)$$

where l_0 represents the minimum logarithm (base 2) of luminance in the scene. The exposure value $v^{(k)}$ is then computed by

$$v^{(k)} = 2^{-l^{(k)}}. \quad (3)$$

Fig. 3 (b)-(d) show the corresponding LDR images, which exhibit different exposures.

¹When photometric units (*e.g.*, luminance) are plotted on the \log_2 axis, each logarithmic unit corresponds to 1 stop.

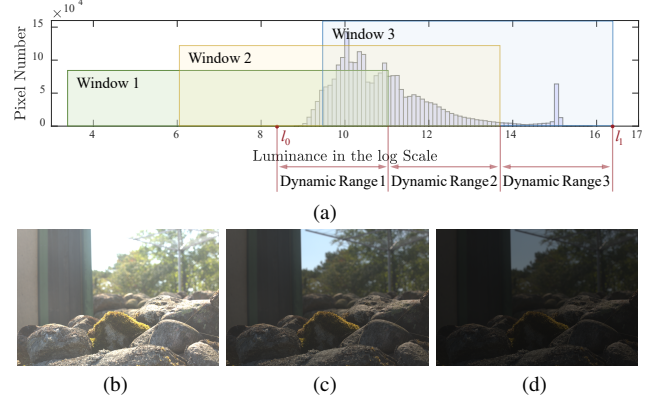


Figure 3. Decomposition an HDR image with eight stops into three LDR images of different exposures using the inverse display model specified in Eq. (1). l_0 and l_1 denote the minimum and maximum luminances in log scale. (a) indicates the positions of the sliding windows according to Eq. (2). (b)-(d) are the LDR images from window 1 to window 3, respectively.

3.2. Quality Assessment Model

Similarly, we may use another set of $\{\hat{v}^{(k)}\}_{k=1}^K$ to compute an LDR image stack $\{\hat{L}^{(k)}\}_{k=1}^K$ for the test HDR image \hat{H} . Then, we are ready to evaluate the perceptual quality of $\hat{L}^{(k)}$ using $L^{(k)}$ as the reference:

$$Q_i^{(k)} = D_i \left(L^{(k)}, \hat{L}^{(k)}; v^{(k)}, \hat{v}^{(k)} \right), \quad (4)$$

where $D(\cdot, \cdot)$ denotes any LDR quality model that produces a local quality, with a higher value indicating better quality. i denotes a pixel index. We pool the local quality scores with a local weighting map:

$$Q^{(k)} = \frac{\sum_i W_i^{(k)} Q_i^{(k)} \left(L^{(k)}, \hat{L}^{(k)}; v^{(k)}, \hat{v}^{(k)} \right)}{\sum_i W_i^{(k)}}, \quad (5)$$

where

$$W_i^{(k)} = \begin{cases} 1 & \text{if } 0.1 \leq L_i^{(k)} \leq 0.9 \\ 0 & \text{otherwise,} \end{cases} \quad (6)$$

is determined by a simple well-exposedness measure to exclude both under- and over-exposed regions (see Fig. 4). The overall quality score is computed by aggregating global quality estimates across exposures:

$$Q = \sum_{k=1}^K G^{(k)} Q^{(k)} \left(L^{(k)}, \hat{L}^{(k)}; v^{(k)}, \hat{v}^{(k)} \right), \quad (7)$$

where $G^{(k)}$ is the k -th global non-negative weighting, and $\sum_k G^{(k)} = 1$. It is flexible to put more emphasis on assessing a certain luminance range by increasing the corresponding $G^{(k)}$. Without otherwise specified, we set $G^{(k)} = 1/K$.

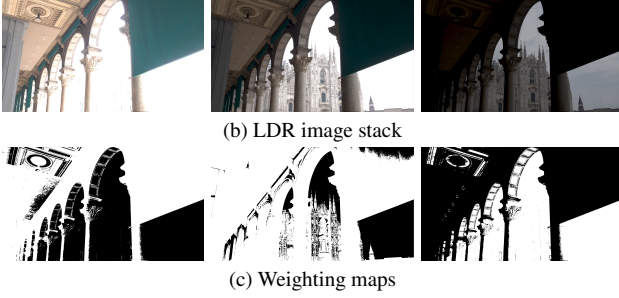


Figure 4. LDR image stack generated by the inverse display model (in Eq. (1)) and the corresponding local weighting maps (by Eq. (6)) for the “Corridor” scene by courtesy of Mark Fairchild [15].

For HDR-to-HDR image processing applications, such as HDR image compression and super-resolution, it is reasonable to set $\hat{v}^{(k)} = v^{(k)}$, for $1 \leq k \leq K$ because there exists little luminance shift between the reference and test HDR images. However, this is not the case for LDR-to-HDR image processing applications like SI-HDR reconstruction and HDR novel view synthesis from LDR views, in which the level of luminance shift will significantly bias the quality assessment results, as observed by Hanji *et al.* [18]. To mitigate this issue, we opt to further maximize Q in Eq. (7) with respect to $\{\hat{v}^{(k)}\}_{k=1}^K$:

$$Q^* = \max_{\{\hat{v}^{(k)}\}_{k=1}^K} Q \left(\{L^{(k)}, \hat{L}^{(k)}; v^{(k)}, \hat{v}^{(k)}\}_{k=1}^K \right), \quad (8)$$

which can be decomposed into K one-dimensional optimization problems, and solved efficiently by gradient-based optimizers. Fig. 5 shows a visualization, where we see the luminance shift is clearly compensated after optimization.

3.3. Discussion

The proposed quality model naturally reduces to the original LDR metric ($D_i(\cdot)$, from Eq. 4) when used with LDR images. This is because the LDR images would need to be first transformed from display-encoded color space (*e.g.* sRGB) to linear color values through the forward display model. The combination of such a forward display model with the inverse display model from Eq. 1 will result in an identity function and, therefore, no change to the input LDR image.

The proposed HDR quality models can also serve as the loss functions for perceptual optimization of HDR image processing systems. In this case, we set $\hat{v}^{(k)} = v^{(k)}$, for $1 \leq k \leq K$, to faithfully reproduce the luminance distribution of the reference HDR image, rather than optimizing $\{\hat{v}^{(k)}\}$ (using Eq. (8)), whose gradient is expensive to compute.

The limitation of the proposed metric is that it does not account for the reduced sensitivity of the visual system at low luminance, *i.e.* the predictions are the same regardless

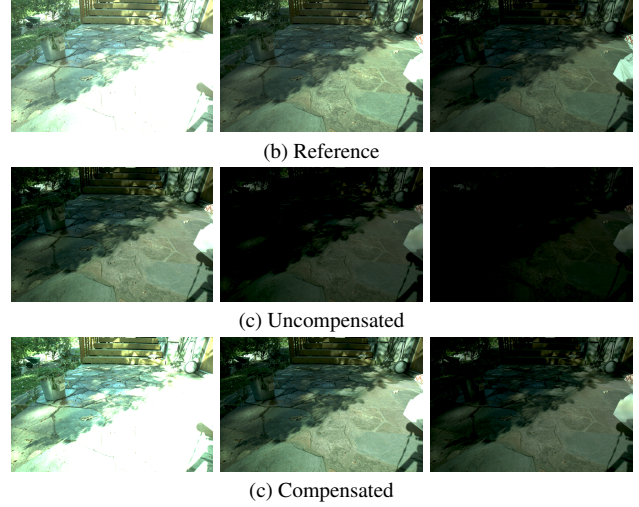


Figure 5. Illustration of compensation for the luminance shift through Eq. (8). (a) LDR image stack generated from the reference HDR image. (b) LDR image stack generated from the HDR image produced by MaskHDR [55] with the same exposure values used in (a). (c) LDR image stack generated from the HDR image produced by MaskHDR [55] with optimized exposure values by Eq. (8). Source image by courtesy of Param Hanji [18].

of whether the image is meant to be shown on a dark or bright display. PU, PU21 transforms, and HDR-VDP metrics model the changes in sensitivity with absolute luminance levels.

4. Experimental Validation

In this section, we present the experimental setups of the proposed family of HDR quality models. We then compare our methods with model-based and encoding-based HDR quality models on four HDR image datasets.

4.1. Experimental Setups

Implementation Details. We adopt five representative LDR quality methods as base models to implement $D(\cdot, \cdot)$ in Eq. (4): mean absolute error (MAE), PSNR, SSIM, the learned perceptual image patch similarity (LPIPS) model [68] with VGGNet [58], and the deep image structure and texture similarity (DISTS) metric [13]. To solve the K one-dimensional optimization problem in Eq. (8), we employ the basic gradient ascent method with an initial learning rate of 10^{-3} , and decay the learning rate by a factor of 5 for every 1,000 iteration, and we train for a maximum of 5,000 iterations. Early stopping is enabled if the loss difference between two consecutive iterations is less than 0.001.

Datasets. Four publicly available HDR image datasets are adopted for benchmarking: Narwaria2013 [44], Valenzise2014 [61], Zerman2017 [67], and UPIQ [38], which contain 140, 50, 100 and 4,159 images, respectively. Of

Table 1. Performance comparison in terms of SRCC and PLCC of the proposed HDR quality models against sixteen competing methods on four HDR datasets. The left and right numbers separated by “/” indicate the performance on the whole UPIQ dataset and its HDR image subset, respectively. The weightings to compute the results in the last column are proportion to the numbers of HDR images in respective datasets. The top-2 results are highlighted in bold

| Model | Narwaria2013 [44] | | Valenzise2014 [61] | | Zerman2017 [67] | | UPIQ [38] | | Weighted Avg | |
|---------------|-------------------|--------------|--------------------|--------------|-----------------|--------------|---------------------|---------------------|--------------|--------------|
| | SRCC | PLCC | SRCC | PLCC | SRCC | PLCC | SRCC | PLCC | SRCC | PLCC |
| NLPD | 0.716 | 0.747 | 0.828 | 0.845 | 0.752 | 0.755 | 0.817/0.814 | 0.833/0.821 | 0.785 | 0.797 |
| HDR-VQM | 0.761 | 0.788 | 0.865 | 0.892 | 0.762 | 0.774 | 0.788/0.818 | 0.817/0.819 | 0.801 | 0.812 |
| HDR-VDP-3-Q | 0.742 | 0.770 | 0.835 | 0.874 | 0.700 | 0.695 | 0.826/ 0.845 | 0.871/ 0.843 | 0.801 | 0.808 |
| HDR-VDP-3-D | 0.723 | 0.735 | 0.829 | 0.854 | 0.700 | 0.708 | 0.801/0.800 | 0.806/0.784 | 0.771 | 0.768 |
| MAE | 0.107 | 0.101 | 0.225 | 0.373 | 0.361 | 0.355 | 0.534/0.256 | 0.570/0.294 | 0.238 | 0.269 |
| PU-MAE | 0.543 | 0.620 | 0.435 | 0.625 | 0.553 | 0.568 | 0.556/0.620 | 0.602/0.639 | 0.579 | 0.623 |
| Improvement | +408.5% | +515.1% | +93.4% | +67.3% | +53.5% | +59.9% | +4.1%/+142.5% | +5.5%/+116.9% | +143.6% | +131.4% |
| PU21-MAE | 0.560 | 0.600 | 0.470 | 0.575 | 0.557 | 0.555 | 0.585/0.613 | 0.625/0.617 | 0.582 | 0.601 |
| Improvement | +424.7% | +496.2% | +108.9% | +53.9% | +54.5% | +56.1% | +9.6%/+139.9% | +9.6%/+109.7% | +145% | +123.3% |
| Q_{MAE}^* | 0.605 | 0.630 | 0.816 | 0.851 | 0.821 | 0.811 | 0.622/0.683 | 0.673/0.690 | 0.698 | 0.708 |
| Improvement | +466.6% | +525.5% | +262.3% | +128.0% | +127.7% | +128.1% | +16.5%/+167.2% | +18.1%/+134.4% | +193.7% | +163.2% |
| PSNR | 0.124 | 0.139 | 0.371 | 0.416 | 0.465 | 0.506 | 0.645/0.299 | 0.650/0.341 | 0.293 | 0.329 |
| PU-PSNR | 0.532 | 0.595 | 0.529 | 0.611 | 0.649 | 0.677 | 0.643/0.631 | 0.651/0.644 | 0.605 | 0.636 |
| Improvement | +327.9% | +326.8% | +42.6% | +46.8% | +39.5% | +33.8% | -0.3%/+111.0% | +0.2%/+88.7% | +106.4% | +93.0% |
| PU21-PSNR | 0.546 | 0.574 | 0.588 | 0.655 | 0.633 | 0.662 | 0.666/0.585 | 0.665/0.591 | 0.584 | 0.603 |
| Improvement | +339.4% | +312.2% | +58.7% | +57.4% | +36.1% | +30.8% | +3.2%/+95.6% | +2.3%/+73.2% | +99.4% | +83.1% |
| Q_{PSNR}^* | 0.655 | 0.695 | 0.808 | 0.858 | 0.859 | 0.863 | 0.695/0.698 | 0.698/0.705 | 0.722 | 0.739 |
| Improvement | +427.5% | +399.2% | +118.0% | +106.2% | +84.7% | +70.5% | +7.7%/+133.5% | +7.4%/+106.6% | +146.5% | +124.3% |
| SSIM | 0.126 | 0.313 | 0.322 | 0.502 | 0.493 | 0.451 | 0.677/0.383 | 0.706/0.475 | 0.341 | 0.440 |
| PU-SSIM | 0.651 | 0.690 | 0.840 | 0.880 | 0.754 | 0.750 | 0.665/0.736 | 0.667/0.738 | 0.729 | 0.741 |
| Improvement | +417.6% | +120.5% | +161.3% | +75.2% | +53.1% | +66.2% | -1.7%/+91.8% | -5.5%/+55.4% | +113.9% | +68.6% |
| PU21-SSIM | 0.633 | 0.679 | 0.837 | 0.863 | 0.757 | 0.744 | 0.680/0.674 | 0.677/0.671 | 0.691 | 0.699 |
| Improvement | +403.3% | +117.0% | +160.2% | +71.8% | +53.8% | +64.8% | +0.5%/+75.8% | -4.1%/+41.2% | +102.8% | +59.0% |
| Q_{SSIM}^* | 0.684 | 0.723 | 0.897 | 0.920 | 0.810 | 0.813 | 0.734/0.755 | 0.747/0.752 | 0.760 | 0.768 |
| Improvement | +443.9% | +131.0% | +178.8% | +83.3% | +64.4% | +80.1% | +8.4%/+96.9% | +5.8%/+58.2% | +122.9% | +74.7% |
| LPIPS | 0.650 | 0.695 | 0.768 | 0.780 | 0.684 | 0.695 | 0.844/0.829 | 0.876/0.824 | 0.765 | 0.774 |
| PU-LPIPS | 0.801 | 0.823 | 0.883 | 0.922 | 0.779 | 0.759 | 0.834/0.832 | 0.870/0.837 | 0.822 | 0.829 |
| Improvement | +23.3% | +18.5% | +15.0% | +18.3% | +13.8% | +9.2% | -1.1%/+0.4% | -0.6%/+1.6% | +7.5% | +7.2% |
| PU21-LPIPS | 0.815 | 0.833 | 0.903 | 0.921 | 0.806 | 0.804 | 0.779/0.822 | 0.838/0.828 | 0.825 | 0.833 |
| Improvement | +25.5% | +19.9% | +17.7% | +18.2% | +17.9% | +15.6% | -7.7%/+0.8% | -4.4%/+0.4% | +7.9% | +7.6% |
| Q_{LPIPS}^* | 0.832 | 0.844 | 0.938 | 0.940 | 0.859 | 0.854 | 0.831/0.834 | 0.880/0.836 | 0.846 | 0.848 |
| Improvement | +28.1% | +21.5% | +22.2% | +20.6% | +25.6% | +22.8% | -1.5%/+0.6% | +0.5%/+1.4% | +10.6% | +9.6% |
| DISTS | 0.515 | 0.593 | 0.794 | 0.848 | 0.811 | 0.846 | 0.860 /0.691 | 0.882 /0.701 | 0.680 | 0.712 |
| PU-DISTS | 0.847 | 0.867 | 0.910 | 0.929 | 0.862 | 0.870 | 0.805/0.788 | 0.857/0.804 | 0.821 | 0.837 |
| Improvement | +64.4% | +46.3% | +14.5% | +9.6% | +6.3% | +2.9% | -6.4%/+14.1% | -2.8%/+14.7% | +20.7% | +17.6% |
| PU21-DISTS | 0.860 | 0.872 | 0.907 | 0.921 | 0.829 | 0.831 | 0.798/0.801 | 0.854/0.822 | 0.826 | 0.842 |
| Improvement | +66.8% | +47.1% | +14.2% | +8.6% | +2.3% | -1.8% | -7.2%/+15.9% | -3.1%/+17.3% | +21.4% | +18.3% |
| Q_{DISTS}^* | 0.916 | 0.913 | 0.927 | 0.939 | 0.910 | 0.913 | 0.864 /0.843 | 0.895 /0.852 | 0.875 | 0.881 |
| Improvement | +77.7% | +54.0% | +16.7% | +10.7% | +12.2% | +7.9% | +0.5%/+22.0% | +1.5%/+21.6% | +28.6% | +23.8% |

particular interest is the UPIQ dataset, which is a combination of 380 HDR images and 3,779 LDR images from a total of four sub-datasets [23, 44, 51, 56] with careful perceptual scale re-alignment.

Competing Metrics. We select four model-based quality models for comparison, including four HDR ones: 1) NLPD [24], 2) HDR-VQM [47], 3) the quality score of HDR-VDP-3 [36] (denoted by HDR-VDP-3-Q) and 4) the difference score of HDR-VDP-3 [36] (denoted by HDR-VDP-3-D), and five LDR ones: 5) MAE, 6) PSNR, 7) SSIM [64], 8) LPIPS [68] and 9) DISTS [13]. We also equip the four LDR quality models with the PU [1] and PU21 encoding, giving rise to 10) PU-MAE, 11) PU-PSNR, 12) PU-SSIM, 13) PU-LPIPS, 14) PU-DISTS, 15) PU21-MAE,

16) PU21-PSNR, 17) PU21-SSIM, 18) PU21-LPIPS, and 19) PU21-DISTS. We assume a test HDR display model with a maximum luminance of 1,000 and 4,000 cd/m² for the PU and PU21 encoding, respectively, as suggested in [1, 30, 34]. We find empirically that the performance ranking of the competing methods is robust to the selection of the maximum luminance of the displays. Meanwhile, we adjust² the hyperparameters of the adopted metrics if necessary. When applying HDR-quality models, PU/PU21 encoding to LDR images in UPIQ, we first convert the digital

²For example, in vanilla SSIM, the two normalizing constants are adjusted to $C_1 = (0.01 \times 4000)^2 = 1,600$ and $C_2 = (0.03 \times 4000)^2 = 14,400$, respectively, when the maximum luminance is 4,000 cd/m².

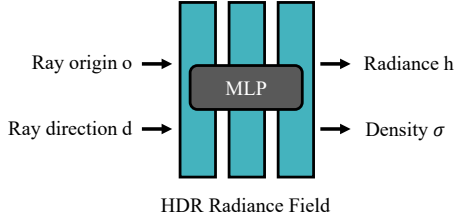


Figure 6. The inputs and outputs of the MLP to implicitly model the HDR radiance field. Image adapted from [21].

pixel values to luminance values via the display model:

$$L = (1 - b)P^\gamma + b \quad \text{and} \quad \hat{L} = (1 - b)\hat{P}^\gamma + b, \quad (9)$$

where P and \hat{P} are digital pixel values of the reference and test LDR images, respectively. The gamma parameter γ and black-level factor b are the same as in Eq. (1). The maximum luminance of L and \hat{L} are scaled to 200 cd/m^2 .

Evaluation Metrics. We employ two evaluation metrics to compare the performance of the IQA models: Spearman’s rank correlation coefficient (SRCC) and Pearson linear correlation coefficient (PLCC). As a standard practice [56, 63], We fit a four-parameter logistic function before computing PLCC.

4.2. Main Results

Table 1 presents the performance comparison of the competing IQA models on four datasets. The immediate observation is that the adopted inverse display model leads to consistent improvements for all base IQA models. In particular, the instantiation Q_{DISTS}^* achieves the best results on all four datasets, even surpassing HDR-VDP-3 on UPIQ, against which HDR-VDP-3 has been re-calibrated. Aligning with previous studies [1, 30], PU and PU21 encoding are able to boost the HDR quality assessment performance of base quality measures, but the improvements are less impressive than our methods, which do not require subjective data for re-calibration. However, when applied to LDR images in UPIQ, PU and PU21 encoding incur noticeable performance degradation. This is in stark contrast with our family of HDR quality models, which preserve the LDR quality assessment capabilities with minimal modifications. Last, there is a clear trend that a better base model generally gives better performance, confirming our original goal of transferring the advances in LDR IQA to assessing HDR images.

5. Perceptual Optimization Applications

In this section, we explore the use of the proposed HDR quality models for perceptual optimization of HDR novel view synthesis.

5.1. HDR Novel View Synthesis

We select HDR-NeRF [21] as the starting point. The original HDR-NeRF uses an MLP to implicitly model the radiance field of an HDR scene, and uses another MLP as the tone mapper to match multiple input LDR images of different exposures. Here, we simplify HDR-NeRF by stripping off the tone mapper, and directly operate in the LDR-to-HDR domain guided by the proposed HDR quality model (see Fig. 6). We denote the simplified method by HDR-NeRF \dagger .

5.1.1 Design of HDR-NeRF \dagger

Network Design. We employ an eight-layer MLP with 256 channels to model the HDR scene radiance. For a given ray $r = o + sd$, where o is the origin, d is the ray direction, and s denotes a position along the ray, the MLP outputs the radiance h and densities σ , based on which a luminance value can be computed by

$$\hat{H}(r) = \int_{s_n}^{s_f} T(s)\sigma(r(s))h(r(s))ds, \quad (10)$$

$$T(s) = \exp\left(-\int_{s_n}^s \sigma(r(v))dv\right). \quad (11)$$

s_n and s_f denote the near and far boundary of the ray, respectively. $T(s)$ denotes the accumulated transmittance along the ray from s_n to s .

Loss Function. We adopt the proposed HDR quality model, Q_{MAE}^* , as the loss function to encourage high-fidelity novel view synthesis at all luminance levels. This is different from that in [21], where LDR images are used as supervision, which requires another MLP as the tone mapper to be learned.

5.1.2 Experiments

Model Training and Testing. We employ the HDR dataset proposed by Huang *et al.* [21] that contains 8 synthetic scenes rendered by Blender³. There are 35 HDR views with different poses for each scene. We select 18 views at different poses as the training set, while the other 17 poses are the test dataset.

The training process is the same as that in the paper [21]. We employ the positional encoding in [40] for the origin and the direction of rays to represent high-frequency variations in color and geometry. Also, we simultaneously optimize the coarse and fine models, where the densities predicted by the coarse model are used to bias the sampling of a ray in the fine model. We sample 64 points along each ray in the coarse model and 128 points in the fine model. We employ

³<https://www.blender.org/>

Table 2. Average quantitative results of HDR novel view synthesis methods on eight synthetic scenes

| Method | HDR-VDP-3-Q | PSNR | SSIM | Without CRF correction | | With CRF correction | | Q^* (Our metric) | |
|--------------------|--------------|---------------|--------------|------------------------|--------------|---------------------|--------------|--------------------|--------------|
| | | | | PU21-PSNR | PU21-SSIM | PU21-PSNR | PU21-SSIM | Q_{PSNR}^* | Q_{SSIM}^* |
| HDR-NeRF | 7.023 | 25.513 | 0.863 | 31.388 | 0.901 | 38.485 | 0.929 | 28.957 | 0.899 |
| HDR-NeRF+ | 9.634 | 27.358 | 0.929 | 35.758 | 0.953 | 41.350 | 0.957 | 32.457 | 0.937 |
| HDR-NeRF \dagger | 9.863 | 28.754 | 0.933 | 38.202 | 0.967 | 43.483 | 0.973 | 34.539 | 0.968 |

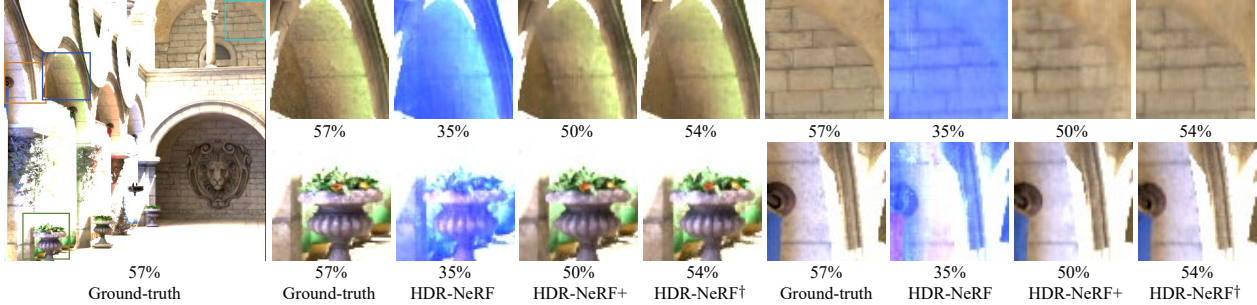


Figure 7. Comparison of HDR-NeRF \dagger with the competing methods on the ‘‘Sponza’’ scene.

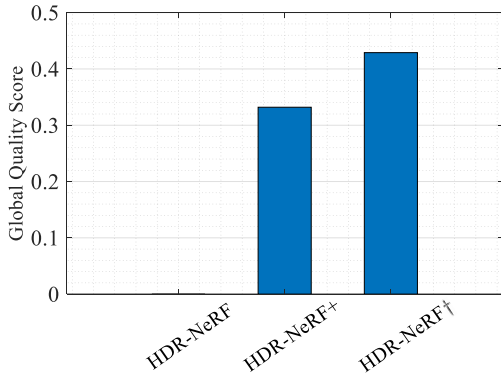


Figure 8. Subjective quality scores across all tested images and observers for the compared HDR novel view synthesis methods in a 2AFC subjective user study.

Adam optimizer [22] as the optimizer with an initial learning rate 5×10^{-4} , which decays exponentially to 5×10^{-5} over the course of optimization. The batch size of rays is set to 1,024. We optimize a single model for 200K iterations. The resolution of each view is 400×400 .

Competing Methods. We compare our method against the original HDR-NeRF [21] and its variant optimized for HDR views directly, which is denoted by HDR-NeRF+. As implementation in [21], when training the HDR-NeRF+ model, the predicted and reference HDR values are tone mapped to LDR values by a simple global tone mapper [52].

Evaluation Metrics. We employ several objective quality metrics: 1) HDR-VDP-3-Q [36] 2) PSNR, 3) SSIM [64], 4) PU21-PSNR, 5) PU21-SSIM, 6) PU21-PSNR with CRF correction [18], 7) PU21-SSIM with CRF correction, 8)

proposed quality metric with PSNR as the base model (*i.e.*, Q_{PSNR}^*), and 9) proposed quality metric with SSIM as the base model (*i.e.*, Q_{SSIM}^*). CRF correction compensates for the metric sensitivity to the shifts in tone and color that are otherwise insensitive to the HVS [14], and is applied before PU21 encoding.

Quantitative Evaluation. The average quantitative results of rendered novel HDR views of the eight synthetic scenes are shown in Table 2, which demonstrates that our method performs the best. The improved results of the proposed HDR-NeRF \dagger over HDR-NeRF+ indicate the superiority of the adopted inverse display model over the simple tone mapper. Lack of direct supervision, the original HDR-NeRF performs marginally in synthesizing HDR views, despite its ability to reconstruct a satisfying output LDR image with the optimized tone mapper network. Quantitative results for every synthetic scene are in supplement.

Qualitative Evaluation. Fig. 7 compares the results on a test view of the ‘‘Sponza’’ scene. The HDR view synthesized by the original HDR-NeRF suffers from color cast and detail loss. More details can be recovered by HDR-NeRF+, but not as sharp as those by the proposed HDR-NeRF \dagger . This shows the advantage of direct supervision in the HDR domain by the proposed HDR quality model.

Subjective User Study. We perform a subjective user study to verify the perceptual advantages of HDR-NeRF \dagger . We invite 15 participants, including 8 males and 7 females aged between 20 and 30. All subjects have general knowledge of image processing but are blind to the detailed purpose of this study. To relieve fatigue, participants are allowed to take a break at any time during subjective testing. For each of the eight scenes, we randomly choose five test

Table 3. Quantitative results of HDR-NeRF† optimized by different loss functions

| Method | HDR-VDP-3-Q | PSNR | SSIM | Without CRF correction | | With CRF correction | | Q^* (Our metric) | |
|--------------------|--------------|---------------|--------------|------------------------|--------------|---------------------|--------------|---------------------|---------------------|
| | | | | PU21-PSNR | PU21-SSIM | PU21-PSNR | PU21-SSIM | Q_{PSNR}^* | Q_{SSIM}^* |
| MAE | 6.224 | 17.181 | 0.454 | 25.842 | 0.613 | 31.577 | 0.856 | 22.928 | 0.849 |
| PU21-MAE | 9.717 | 28.670 | 0.929 | 37.293 | 0.960 | 42.245 | 0.970 | 33.477 | 0.949 |
| log-MAE | 9.720 | 23.173 | 0.840 | 34.006 | 0.936 | 41.267 | 0.961 | 32.423 | 0.944 |
| μ -MAE | 9.784 | 25.645 | 0.894 | 35.408 | 0.948 | 42.104 | 0.968 | 33.227 | 0.948 |
| Q_{MAE}^* | 9.863 | 28.754 | 0.933 | 38.202 | 0.967 | 43.483 | 0.973 | 34.539 | 0.968 |

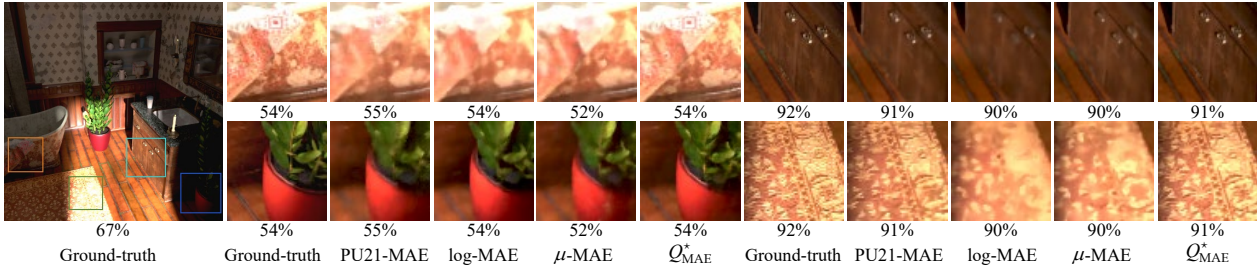


Figure 9. Comparison of HDR-NeRF† optimized by different loss functions on the ‘‘Bathroom’’ scene.

views, each of which is reconstructed by the three competing methods (including HDR-NeRF†). We manually select $\{v^{(k)}\}_{k=1}^3$ to zoom in the low, middle, and high luminance range of each reference HDR image, respectively. All LDR images are aligned to the reference LDR images by solving Eq. (8). We adopt the 2AFC approach to gather human preferences of $\binom{3}{2} \times 8 \times 5 \times 3 = 360$ image pairs. Participants are given unlimited time to look at the images and to make their decisions. The global quality scores are also obtained by the maximum likelihood estimation based on the assumption that the quality value obeys the Thurstone’s model [60]. The results are shown in Fig. 8, which demonstrates that HDR-NeRF† indeed offers the best perceptual results.

Ablation study. We compare the view synthesis performance of HDR-NeRF† optimized by several different objective quality metrics: 1) MAE, 2) PU21-MAE, 3) log encoded MAE (log-MAE), 4) MAE computed in the tone mapped domain via the μ -law (μ -MAE), and 5) the proposed Q_{MAE}^* .

Table 3 shows the quantitative comparison results, where HDR-NeRF† optimized by Q_{MAE}^* outperforms those optimized by other quality models as loss functions. The encoding-based metrics like PU21-MAE and log-MAE are not necessarily better than μ -MAE, even if tone mapping will result in detail loss and color distortion. We also visually compare different loss functions on a test view of the ‘‘Bathroom’’ scene in Fig. 9. It can be observed that HDR-NeRF† optimized by Q_{MAE}^* gives the best synthesis results, in terms of detail and tone reproduction in all luminance levels.

6. Conclusion and Discussion

We have described a family of HDR quality models by augmenting current LDR quality metrics with a simple inverse display model, without the need of HDR subjective data for re-calibration. We have validated the proposed quality models in terms of correlation with MOSs on four HDR IQA datasets and optimization of HDR novel view synthesis.

We have noticed that the previous objective evaluation of HDR novel view synthesis methods was implemented rather differently and inconsistently. To fully justify the perceptual improvements brought by the proposed HDR quality models, we thus gave a careful treatment of objective quality evaluation by 1) adjusting the hyper-parameters of adopted quality metrics (*e.g.*, SSIM) accordingly based on the specified HDR display model, and 2) leveraging PU encoding [30] and CRF correction [18].

Previous studies regarding HDR image processing are inclined to adopt a global tone mapper for visualizing and comparing the processed results. In this paper, we advocated a different way of accomplishing the same goal with the inverse display model in Eq. (1), which gives us an opportunity to focus on and enhance the visibility of different portions of luminance ranges for more tangible visual comparison. Together with the proposed family of HDR quality models, we expect more rapid and reliable progress of HDR related fields in the near future.

References

- [1] Tunç O. Aydın, Rafał K. Mantiuk, and Hans-Peter Seidel. Extending quality metrics to full luminance range images. In

- Human Vision and Electronic Imaging XIII*, pages 109–118, 2008.
- [2] Jonathan T Barron, Ben Mildenhall, Matthew Tancik, Peter Hedman, Ricardo Martin-Brualla, and Pratul P Srinivasan. Mip-NeRF: A multiscale representation for anti-aliasing neural radiance fields. In *IEEE International Conference on Computer Vision*, pages 5855–5864, 2021.
- [3] Jonathan T. Barron, Ben Mildenhall, Dor Verbin, Pratul P. Srinivasan, and Peter Hedman. Mip-NeRF 360: Unbounded anti-aliased neural radiance fields. In *IEEE Conference on Computer Vision and Pattern Recognition*, pages 5460–5469, 2022.
- [4] Peter G. J. Barten. Formula for the contrast sensitivity of the human eye. In *Image Quality and System Performance*, pages 231 – 238, 2003.
- [5] Mark Boss, Raphael Braun, Varun Jampani, Jonathan T Barron, Ce Liu, and Hendrik Lensch. NeRD: Neural reflectance decomposition from image collections. In *IEEE International Conference on Computer Vision*, pages 12684–12694, 2021.
- [6] Chris Buehler, Michael Bosse, Leonard McMillan, Steven Gortler, and Michael Cohen. Unstructured lumigraph rendering. In *Annual Conference on Computer Graphics and Interactive Techniques*, pages 425–432, 2001.
- [7] Matteo Carandini and David J Heeger. Normalization as a canonical neural computation. *Nature Reviews Neuroscience*, 13(1):51–62, 2012.
- [8] Anpei Chen, Zexiang Xu, Fuqiang Zhao, Xiaoshuai Zhang, Fanbo Xiang, Jingyi Yu, and Hao Su. MVNeRF: Fast generalizable radiance field reconstruction from multi-view stereo. In *IEEE International Conference on Computer Vision*, pages 14124–14133, 2021.
- [9] Xingyu Chen, Qi Zhang, Xiaoyu Li, Yue Chen, Ying Feng, Xuan Wang, and Jue Wang. Hallucinated neural radiance fields in the wild. In *IEEE Conference on Computer Vision and Pattern Recognition*, pages 12943–12952, 2022.
- [10] Zhang Chen, Anpei Chen, Guli Zhang, Chengyuan Wang, Yu Ji, Kiriakos N Kutulakos, and Jingyi Yu. A neural rendering framework for free-viewpoint relighting. In *IEEE Conference on Computer Vision and Pattern Recognition*, pages 5599–5610, 2020.
- [11] Inchang Choi, Orazio Gallo, Alejandro Troccoli, Min H Kim, and Jan Kautz. Extreme view synthesis. In *IEEE International Conference on Computer Vision*, pages 7781–7790, 2019.
- [12] Scott J. Daly. Visible differences predictor: An algorithm for the assessment of image fidelity. In *Human Vision, Visual Processing, and Digital Display III*, pages 2–15, 1992.
- [13] Keyan Ding, Kede Ma, Shiqi Wang, and Eero P. Simoncelli. Image quality assessment: Unifying structure and texture similarity. *IEEE Transactions on Pattern Analysis and Machine Intelligence*, 44(5):2567–2581, 2022.
- [14] Gabriel Eilertsen, Saghi Hajisharif, Param Hanji, Apostolia Tsirikoglou, Rafał K. Mantiuk, and Jonas Unger. How to cheat with metrics in single-image HDR reconstruction. In *IEEE International Conference on Computer Vision Workshops*, pages 3998–4007, 2021.
- [15] Mark D. Fairchild. The HDR photographic survey. In *Color and Imaging Conference*, pages 233–238, 2007.
- [16] John Flynn, Michael Broxton, Paul Debevec, Matthew DuVall, Graham Fyffe, Ryan Overbeck, Noah Snavely, and Richard Tucker. DeepView: View synthesis with learned gradient descent. In *IEEE Conference on Computer Vision and Pattern Recognition*, pages 2367–2376, 2019.
- [17] Steven J. Gortler, Radek Grzeszczuk, Richard Szeliski, and Michael F. Cohen. The lumigraph. In *Annual Conference on Computer Graphics and Interactive Techniques*, pages 43–54, 1996.
- [18] Param Hanji, Rafał K. Mantiuk, Gabriel Eilertsen, Saghi Hajisharif, and Jonas Unger. Comparison of single image HDR reconstruction methods — the caveats of quality assessment. In *Annual Conference on Computer Graphics and Interactive Techniques*, pages 1:1–1:8, 2022.
- [19] Peter Hedman, Julien Philip, True Price, Jan-Michael Frahm, George Drettakis, and Gabriel Brostow. Deep blending for free-viewpoint image-based rendering. *ACM Transactions on Graphics*, 37(6):257:1–257:15, 2018.
- [20] Bernd Hoefflinger. *High-Dynamic-Range (HDR) Vision*. Springer, 2007.
- [21] Xin Huang, Qi Zhang, Ying Feng, Hongdong Li, Xuan Wang, and Qing Wang. HDR-NeRF: High dynamic range neural radiance fields. In *IEEE Conference on Computer Vision and Pattern Recognition*, pages 18398–18408, 2022.
- [22] Diederik P Kingma and Jimmy Ba. Adam: A method for stochastic optimization. *arXiv preprint arXiv:1412.6980*, 2014.
- [23] Pavel Korshunov, Philippe Hanhart, Thomas Richter, Alessandro Artusi, Rafał K. Mantiuk, and Touradj Ebrahimi. Subjective quality assessment database of HDR images compressed with JPEG XT. In *International Workshop on Quality of Multimedia Experience*, pages 1–6, 2015.
- [24] Valero Laparra, Alex Berardino, Johannes Ballé, and Eero P Simoncelli. Perceptually optimized image rendering. *Journal of the Optical Society of America A*, 34(9):1511–1525, 2017.
- [25] Marc Levoy and Pat Hanrahan. Light field rendering. In *Annual Conference on Computer Graphics and Interactive Techniques*, pages 31–42, 1996.
- [26] Zhengqi Li, Simon Niklaus, Noah Snavely, and Oliver Wang. Neural scene flow fields for space-time view synthesis of dynamic scenes. In *IEEE Conference on Computer Vision and Pattern Recognition*, pages 6498–6508, 2021.
- [27] Steven Liu, Xiuming Zhang, Zhoutong Zhang, Richard Zhang, Jun-Yan Zhu, and Bryan Russell. Editing conditional radiance fields. In *IEEE International Conference on Computer Vision*, pages 5773–5783, 2021.
- [28] Stephen Lombardi, Tomas Simon, Jason Saragih, Gabriel Schwartz, Andreas Lehrmann, and Yaser Sheikh. Neural volumes: Learning dynamic renderable volumes from images. *ACM Transactions on Graphics*, 38(4):65:1–65:14, 2019.
- [29] Li Ma, Xiaoyu Li, Jing Liao, Qi Zhang, Xuan Wang, Jue Wang, and Pedro V Sander. Deblur-NeRF: Neural radiance fields from blurry images. In *IEEE Conference on Computer Vision and Pattern Recognition*, pages 12861–12870, 2022.

- [30] Rafał K. Mantiuk and Maryam Azimi. PU21: A novel perceptually uniform encoding for adapting existing quality metrics for HDR. In *Picture Coding Symposium*, pages 1–5, 2021.
- [31] Rafał K. Mantiuk and Wolfgang Heidrich. Visualizing high dynamic range images in a web browser. *Journal of Graphics, GPU, and Game Tools*, 14(1):43–53, 2009.
- [32] Rafał K. Mantiuk and Giovanni (Gianni) Ramponi. Age-dependent prediction of visible differences in displayed images: Age-dependent prediction of visible differences. *Journal of the Society for Information Display*, 26:1–21, 2018.
- [33] Rafał K. Mantiuk, Scott J. Daly, Karol Myszkowski, and Hans-Peter Seidel. Predicting visible differences in high dynamic range images: Model and its calibration. In *Human Vision and Electronic Imaging X*, pages 204–214, 2005.
- [34] Rafał K. Mantiuk, Kil Joong Kim, Allan G. Rempel, and Wolfgang Heidrich. HDR-VDP-2: A calibrated visual metric for visibility and quality predictions in all luminance conditions. *ACM Transactions On Graphics*, 30(4):40:1–40:14, 2011.
- [35] Rafał K. Mantiuk, Minjung Kim, Maliha Ashraf, Qiang Xu, M. Ronnier Luo, Jasna Martinovic, and Sophie Wuerger. Practical color contrast sensitivity functions for luminance levels up to 10000 cd/m². In *Color and Imaging Conference*, pages 28:1–28:6, 2020.
- [36] Rafał K. Mantiuk, Dounia Hammou, and Param Hanji. HDR-VDP-3: A multi-metric for predicting image differences, quality and contrast distortions in high dynamic range and regular content. *arXiv preprint arXiv:2304.13625*, 2023.
- [37] Ricardo Martin-Brualla, Noha Radwan, Mehdi SM Sajjadi, Jonathan T Barron, Alexey Dosovitskiy, and Daniel Duckworth. NeRF in the wild: Neural radiance fields for unconstrained photo collections. In *IEEE Conference on Computer Vision and Pattern Recognition*, pages 7210–7219, 2021.
- [38] Aliaksei Mikhailiuk, María Pérez-Ortiz, Dingcheng Yue, Wilson Suen, and Rafał K. Mantiuk. Consolidated dataset and metrics for high-dynamic-range image quality. *IEEE Transactions on Multimedia*, 24(67):2125–2138, 2021.
- [39] Ben Mildenhall, Pratul P Srinivasan, Rodrigo Ortiz-Cayon, Nima Khademi Kalantari, Ravi Ramamoorthi, Ren Ng, and Abhishek Kar. Local light field fusion: Practical view synthesis with prescriptive sampling guidelines. *ACM Transactions on Graphics*, 38(4):29:1–29:14, 2019.
- [40] Ben Mildenhall, Pratul P. Srinivasan, Matthew Tancik, Jonathan T. Barron, Ravi Ramamoorthi, and Ren Ng. NeRF: Representing scenes as neural radiance fields for view synthesis. *Communications of the ACM*, 65(1):99–106, 2021.
- [41] Ben Mildenhall, Peter Hedman, Ricardo Martin-Brualla, Pratul P Srinivasan, and Jonathan T Barron. NeRF in the dark: High dynamic range view synthesis from noisy raw images. In *IEEE Conference on Computer Vision and Pattern Recognition*, pages 16190–16199, 2022.
- [42] Scott Miller, Mahdi Nezamabadi, and Scott Daly. Perceptual signal coding for more efficient usage of bit codes. *SMPTE Motion Imaging Journal*, 122(4):52–59, 2013.
- [43] Jacob Munkberg, Petrik Clarberg, Jon Hasselgren, and Tomas Akenine-Möller. High dynamic range texture compression for graphics hardware. *ACM Transactions on Graphics*, 25(3):698–706, 2006.
- [44] Manish Narwaria, Matthieu Perreira Da Silva, Patrick Le Callet, and Romuald Pepion. Tone mapping-based high-dynamic-range image compression: Study of optimization criterion and perceptual quality. *Optical Engineering*, 52(10):102008:1–102008:15, 2013.
- [45] Manish Narwaria, Matthieu Perreira Da Silva, Patrick Le Callet, and Romuald Pepion. Impact of tone mapping in high dynamic range image compression. In *International Workshop on Video Processing and Quality Metrics for Consumer Electronics*, pages 1–7, 2014.
- [46] Manish Narwaria, Rafał K. Mantiuk, Matthieu Perreira Da Silva, and Patrick Le Callet. HDR-VDP-2.2: A calibrated method for objective quality prediction of high-dynamic range and standard images. *Journal of Electronic Imaging*, 24(1):010501:1–010501:10, 2015.
- [47] Manish Narwaria, Matthieu Perreira da Silva, and Patrick Le Callet. HDR-VQM: An objective quality measure for high dynamic range video. *Signal Processing: Image Communication*, 35(4):46–60, 2015.
- [48] Michael Niemeyer and Andreas Geiger. GIRAFFE: Representing scenes as compositional generative neural feature fields. In *IEEE Conference on Computer Vision and Pattern Recognition*, pages 11453–11464, 2021.
- [49] Keunhong Park, Utkarsh Sinha, Jonathan T Barron, Sofien Bouaziz, Dan B Goldman, Steven M Seitz, and Ricardo Martin-Brualla. Nerfies: Deformable neural radiance fields. In *IEEE International Conference on Computer Vision*, pages 5865–5874, 2021.
- [50] Nikolay Ponomarenko, Federica Battisti, Karen Egiazarian, Jaakko Astola, and Vladimir Lukin. Metrics performance comparison for color image database. In *International Workshop on Video Processing and Quality Metrics for Consumer Electronics*, pages 1–6, 2009.
- [51] Nikolay Ponomarenko, Lina Jin, Oleg Ieremeiev, Vladimir Lukin, Karen Egiazarian, Jaakko Astola, Benoit Vozel, Kacem Chehdi, Marco Carli, Federica Battisti, et al. Image database TID2013: Peculiarities, results and perspectives. *Signal Processing: Image Communication*, 30(3):57–77, 2015.
- [52] Erik Reinhard, Michael Stark, Peter Shirley, and James Ferwerda. Photographic tone reproduction for digital images. *ACM Transactions On Graphics*, 21(3):267–276, 2002.
- [53] Gernot Riegler and Vladlen Koltun. Free view synthesis. In *European Conference on Computer Vision*, pages 623–640, 2020.
- [54] Gernot Riegler and Vladlen Koltun. Stable view synthesis. In *IEEE Conference on Computer Vision and Pattern Recognition*, pages 12211–12220, 2021.
- [55] Marcel Santana Santos, Tsang Ing Ren, and Nima Khademi Kalantari. Single image HDR reconstruction using a CNN with masked features and perceptual loss. *ACM Transactions on Graphics*, 39(4):80:1–80:10, 2020.
- [56] H.R. Sheikh, M.F. Sabir, and Alan C. Bovik. A statistical evaluation of recent full reference image quality assessment algorithms. *IEEE Transactions on Image Processing*, 15(11):3440–3451, 2006.

- [57] Harry Shum and Sing Bing Kang. Review of image-based rendering techniques. In *Visual Communications and Image Processing*, pages 2–13, 2000.
- [58] Karen Simonyan and Andrew Zisserman. Very deep convolutional networks for large-scale image recognition. In *International Conference on Learning Representations*, pages 1–14, 2015.
- [59] Vincent Sitzmann, Justus Thies, Felix Heide, Matthias Nießner, Gordon Wetzstein, and Michael Zollhofer. DeepVoxels: Learning persistent 3D feature embeddings. In *IEEE Conference on Computer Vision and Pattern Recognition*, pages 2437–2446, 2019.
- [60] Louis L. Thurstone. A law of comparative judgment. *Psychological Review*, 34(4):273–286, 1927.
- [61] Giuseppe Valenzise, Francesca De Simone, Paul Lauga, and Frederic Dufaux. Performance evaluation of objective quality metrics for HDR image compression. In *Applications of Digital Image Processing XXXVII*, pages 78–87, 2014.
- [62] Peter Vangorp, Karol Myszkowski, Erich W. Graf, and Rafał K. Mantiuk. A model of local adaptation. *ACM Transactions On Graphics*, 34(6):166:1–166:13, 2015.
- [63] VQEG et al. Final report from the video quality experts group on the validation of objective models of video quality assessment. In *Video Quality Experts Group meeting*, 2000.
- [64] Zhou Wang, Alan C. Bovik, Hamid R. Sheikh, and Eero P. Simoncelli. Image quality assessment: From error visibility to structural similarity. *IEEE Transactions on Image Processing*, 13(4):600–612, 2004.
- [65] Ruifeng Xu, Sumanta N. Pattanaik, and Charles E. Hughes. High-dynamic-range still-image encoding in JPEG 2000. *IEEE Computer Graphics and Applications*, 25(6):57–64, 2005.
- [66] Alex Yu, Vickie Ye, Matthew Tancik, and Angjoo Kanazawa. PixelNeRF: Neural radiance fields from one or few images. In *IEEE Conference on Computer Vision and Pattern Recognition*, pages 4578–4587, 2021.
- [67] Emin Zeman, Giuseppe Valenzise, and Frederic Dufaux. An extensive performance evaluation of full-reference HDR image quality metrics. *Quality and User Experience*, 2(5):1–16, 2017.
- [68] Richard Zhang, Phillip Isola, Alexei A Efros, Eli Shechtman, and Oliver Wang. The unreasonable effectiveness of deep features as a perceptual metric. In *IEEE Conference on Computer Vision and Pattern Recognition*, pages 586–595, 2018.
- [69] MI Zhenxing and Dan Xu. Switch-NeRF: Learning scene decomposition with mixture of experts for large-scale neural radiance fields. In *International Conference on Learning Representations*, 2022.
- [70] Tinghui Zhou, Richard Tucker, John Flynn, Graham Fyffe, and Noah Snavely. Stereo magnification: Learning view synthesis using multiplane images. *ACM Transactions on Graphics*, 37(4):65:1–65:12, 2018.